Yi-Hsin Liu,<sup>1</sup> Prayash Pyakurel,<sup>2</sup> Xiaocan Li,<sup>3</sup> Michael Hesse,<sup>4</sup> Naoki Bessho,<sup>5</sup> Kevin Genestreti,<sup>6</sup> and Shiva B. Thapa<sup>1</sup>

Department of Physics and Astronomy, Dartmouth College, Hanover, NH 03750, USA\*
 Space Sciences Laboratory, University of California, Berkeley, CA 94720, USA
 Los Alamos National Laboratory, Los Alamos, NM 87545, USA
 Ames Research Center, NASA, Moffett Field, CA 94035, USA
 Goddard Space Flight Center, NASA, Greenbelt, MD 20771, USA
 Southwest Research Institute, Durham, NH 03824, USA

Abstract: "Electron-only" reconnection, which is both uncoupled from the surrounding ions and much faster than standard reconnection, is arguably ubiquitous in turbulence. One critical step to understanding the rate in this novel regime is to model the outflow speed that limits the transport of the magnetic flux, which is super ion Alfvénic but significantly lower than the electron Alfvén speed based on the asymptotic reconnecting field. Here we develop a simple model to determine this limiting speed by taking into account the multiscale nature of reconnection, the Hall-mediated electron outflow speed, and the pressure buildup within the small system. The predicted scalings of rates and various key quantities compare well with fully kinetic simulations and can be useful for interpreting the observations of NASA's Magnetospheric-Multiscale (MMS) mission and other ongoing missions.

## I. INTRODUCTION

10

Magnetic reconnection converts magnetic energy into 12 plasma thermal and kinetic energy in laboratory, space, and astrophysical plasmas. Recently, NASA's Magnetospheric-Multiscale (MMS) mission [1] discovered novel form of reconnection in the turbulent magneto sheath downstream of Earth's bow shock [2–5]. These reconnection events, characterized by electron-scale current sheets with super ion-Alfvénic electron jets and no ion outflows, were named "electron-only" reconnection. The ions are decoupled from the system because of a limited spatial and temporal span dictated by the scale of turbulence eddies [6–9]. Electron-only reconnection has also been identified in other regions, including the bow shock transition layer [10-12] and its foreshock [13], Earth's magnetotail [14–16], macro-scale magnetic flux ropes [17], reconnection exhausts [18], dipolarization fronts [19], and has been studied in laboratory experiments [20–23]. One pronounced feature of such reconnection events which is not fully understood is their higher rates in processing magnetic flux and releasing magnetic energy than standard reconnection.

Using particle-in-cell (PIC) simulations, Pyakurel et al. (2019) [6] suggested that the transition from standard, ion-coupled reconnection to electron-only reconnection occurs when the system size is smaller than  $\sim \mathcal{O}(10)$  ion-inertial  $(d_i)$  scales, which appears to be consistent with MMS analyses [3, 4]. In another independent numerical study, Guan et al. (2023) [24] showed that the ion gyroradius  $(\rho_i)$  is also critical in controlling this transition.

In light of these PIC simulations, in this work we model the underlying physics that enables the faster flux trans-

42 port in the electron-only regime, namely the electron out-43 flow speed. This speed is not limited by the ion Alfvénic 44 speed when ions are not coupled within the system, unlike that in the standard reconnection. The electron out-46 flow speed not only determines the magnetic flux trans-47 port into the reconnection exhausts but also the geometry 48 surrounding the electron diffusion region (EDR), where 49 the magnetic flux frozen-in condition for electron flows 50 is violated [25–27]. To derive this speed, the analytical 51 model presented here incorporates both the dispersive 52 nature of the electron jets within the Hall regime [28– <sub>53</sub> 30] and the back pressure accumulated at the outflows. 54 We found that both effects are encoded in the in-plane 55 electric field, which is important to the acceleration of 56 electrons. The resulting scalings of various key quanti-57 ties in different system sizes compare well with those in 58 PIC simulations. The leading outcome of this theory is 59 the explanation of why the normalized electron-only re-60 connection rate appears to be bounded by a value  $\simeq \mathcal{O}(1)$ 61 in a closed system, as seen in PIC simulations. Besides, it also predicts a higher upper bound value  $\simeq 4.28$  if the 63 outflow boundary is open.

#### II. RESULTS

To highlight key features critical to the rate determination, we carry out 2D PIC simulations of magnetic reconnection in plasmas of realistic proton-to-electron mass ratio  $m_{\rm i}/m_{\rm e}=1836$ . We employ the setup of case A in Pyakurel et al., (2019) [6] that has a guide field  $B_{\rm g}=-8B_{x0}$ , where  $B_{x0}$  is the reconnecting component. The ion  $\beta_{\rm i}=3.54$  and electron  $\beta_{\rm e}=0.35$ . These are chosen based on the parameters of the MMS electron-only event [2], but with five different system sizes,  $L_x \times L_z=1.28d_{\rm i} \times 2.56d_{\rm i}, 2.56d_{\rm i} \times 2.56d_{\rm i}, 3.84d_{\rm i} \times 3.84d_{\rm i}, 5.12d_{\rm i} \times 5.12d_{\rm i}$  and  $7.68d_{\rm i} \times 7.68d_{\rm i}$ . Details of the sim-

<sup>\*</sup> Yi-Hsin.Liu@Dartmouth.edu

<sup>76</sup> ulations setup are in the "Methods" section. The units <sup>77</sup> used in the presentation include the ion cyclotron time <sup>78</sup>  $\Omega_{\rm ci}^{-1} \equiv (eB_{x0}/m_{\rm i}c)^{-1}$ , the in-plane ion Alfvén speed <sup>79</sup>  $V_{\rm Ai0} = B_{x0}/(4\pi n_0 m_{\rm i})^{1/2}$  based on the upstream density <sup>80</sup>  $n_0$ , and the ion inertial length  $d_{\rm i} \equiv c/(4\pi n_0 e^2/m_{\rm i})^{1/2}$ .

## A. Character of "electron-only" reconnection

PIC simulations capture electron-only reconnection when the domain size is small enough. Figure 1 shows the essential features in the  $L_x = 2.56d_i$  case. The electron outflow speed  $V_{\rm ex}$  (Fig. 1(a)) indicates active transport of reconnected magnetic flux. Unlike in ion-coupled standard reconnection, it is evident that ion outflows  $V_{ix}$  do not develop in Fig. 1(b). Interestingly, electron-only reconnection has a higher reconnection rate than the stanof dard reconnection rate of  $\mathcal{O}(0.1)$  [31–34], as shown in Fig. 1(e). This is somewhat expected because magnetic flux transport is now not limited by the ion Alfvén speed, as in the ion-coupled reconnection, but by the faster electron Alfvén speed since ions are not magnetized/coupled within the small domain. Naively, if the estimate of the typical EDR aspect ratio  $\sim 0.1$  times the ratio of the electron Alfvén speed  $V_{\text{Ae0}} = B_{x0}/(4\pi n_0 m_e)^{1/2}$  and the  $v_{
m S}$ ion Alfvén speed  $v_{
m Ai0}$  is used, we get the normalized re-99 connection rate

$$R \equiv \frac{cE_{\rm R}}{B_{x0}V_{\rm Ai0}} \simeq 0.1 \times \frac{V_{\rm Ae0}}{V_{\rm Ai0}} = 0.1 \times \sqrt{1836} \simeq 4.28 \quad (1)$$

where  $E_{\rm R}$  is the reconnection electric field. Note that, throughout this paper, the subscript "0" is reserved for upstream asymptotic values. This R value, however, is too high compared to the simulation results, as shown in Fig. 1(e). The rate only gets closer to unity  $\mathcal{O}(1)$ , and a scaling law has not been developed yet.

To address this issue, one key observation is that the limiting speed is actually much lower than the asymptotic electron Alfvén speed  $V_{\text{Ae0}}$ . Figure 1(c) shows cuts of the x-direction electron flow velocity  $V_{\rm ex}$  in blue, ion flow ve-110 locity  $V_{ix}$  in red, and the  $E \times B$  drift velocity in black along the midplane (z=0). Electrons reach a peak out-<sub>112</sub> flow speed  $V_{\rm ex,peak} \simeq 0.15 V_{\rm Ae0}$  when they exit the EDR 113 (the red box in Fig. 1(b)). This  $V_{ex,peak}$  value (also shown as the purple horizontal line in Fig. 1(d)) is, instead, close 115 to the electron Alfvén speed based on the local  $B_x$  at the EDR-scale in the nonlinear stage; this can be seen by comparing it with the blue line in Fig. 1(d) near the edge of the red shaded vertical band of  $d_{\rm e}$ -scale. We will denote this relation by  $V_{\rm ex,peak} \sim V_{\rm Ae} \equiv B_{xe}/(4\pi n m_{\rm e})^{1/2}$ . Farther downstream in Fig. 1(c),  $V_{ex}$  plateaus to a 121 super ion Alfvénic value of 1.7V<sub>Ai0</sub> that is only 4% of the asymptotic electron Alfvén speed  $V_{\rm Ae0}$ . This critical speed limits the flux transport. The time evolution of the electron outflow velocity  $V_{ex}$  cuts (Fig. 2(b)), demon-125 strates the development of the plateauing of  $V_{\rm ex}$  after

the reconnection rate also reaches its plateau (Fig. 1(e)).

127 Similar  $V_{\rm ex}$  plateaus (of different values) also develop in

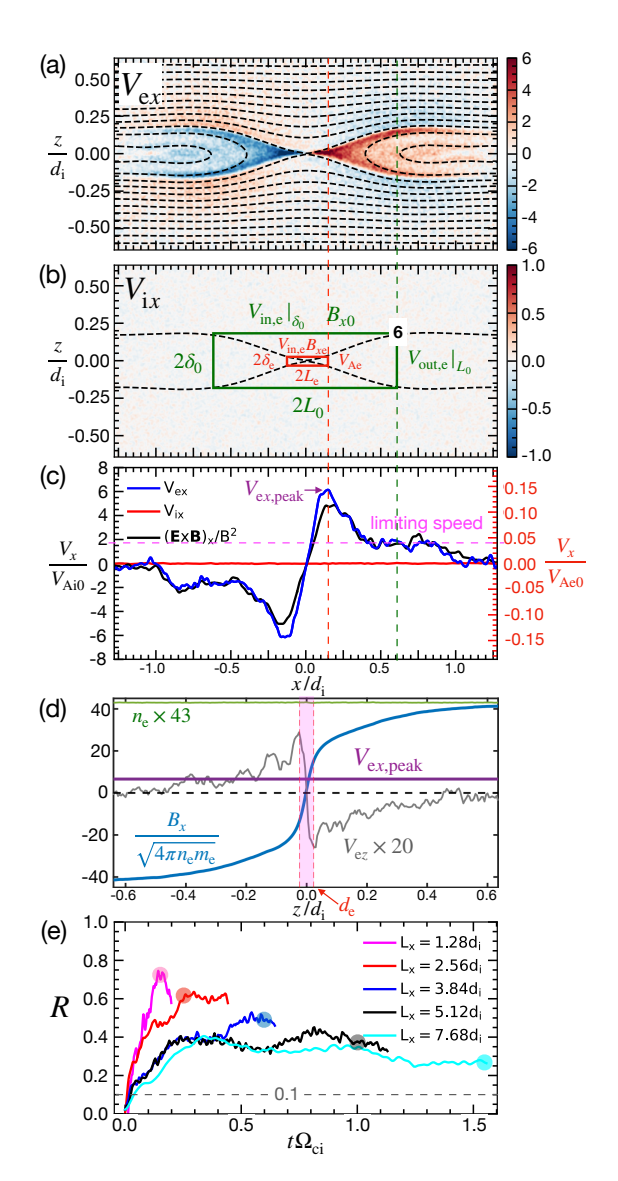


FIG. 1. Key features in the  $L_x = 2.5d_i$  case and recon**nection rates.** (a) Electron outflow speed  $V_{ex}$  overlaid with the contour of the in-plane magnetic flux  $\psi$ . Note that the entire domain is smaller than the typical ion diffusion region (IDR) in standard reconnection. (b) Ion outflow speed  $V_{ix}$ overlaid with the separatrices in dashed black. The red box of size  $2L_e \times 2\delta_e$  marks the electron diffusion region (EDR). The corners (such as point "6") of the green box of size  $2L_0 \times 2\delta_0$ mark the locations downstream of which the exhaust opening angle quickly decreases to 0. (c) Cuts of  $V_{ex}$ ,  $V_{ix}$  and the  $E \times B$  drift speed along the z = 0 line. The (red and green) dashed vertical lines mark the outflow boundaries of the EDR and the green box in (b), while the magenta dashed horizontal line denotes the limiting speed. (d) In blue the electron Alfvén speed based on the local  $B_x$  and  $n_e$  as a function of z at x = 0. In gray the electron inflow speed  $V_{ez} \times 20$ . In green the electron density  $n_{\rm e} \times 43$ . In purple the peak velocity  $V_{\text{ex,peak}}$  from (c). The red shaded band marks the EDR. (e) Reconnection rate R as a function of time for simulations of different system sizes. The rates in our simulations are computed from  $R = (\partial \Delta \psi / \partial t) / B_{x0} V_{Ai0}$  where  $\Delta \psi$  is the magnetic flux difference between the X-line and the O-line. Note that  $\partial \Delta \psi / \partial t = c E_{\rm R}$ , the reconection electric field, in 2D systems. The gray dashed horizontal line indicates the typical rate of ion-coupled standard reconnection [31]. The transparent color circles mark the time of these  $V_{\mathrm{e}x}$  contours in Fig. 2.

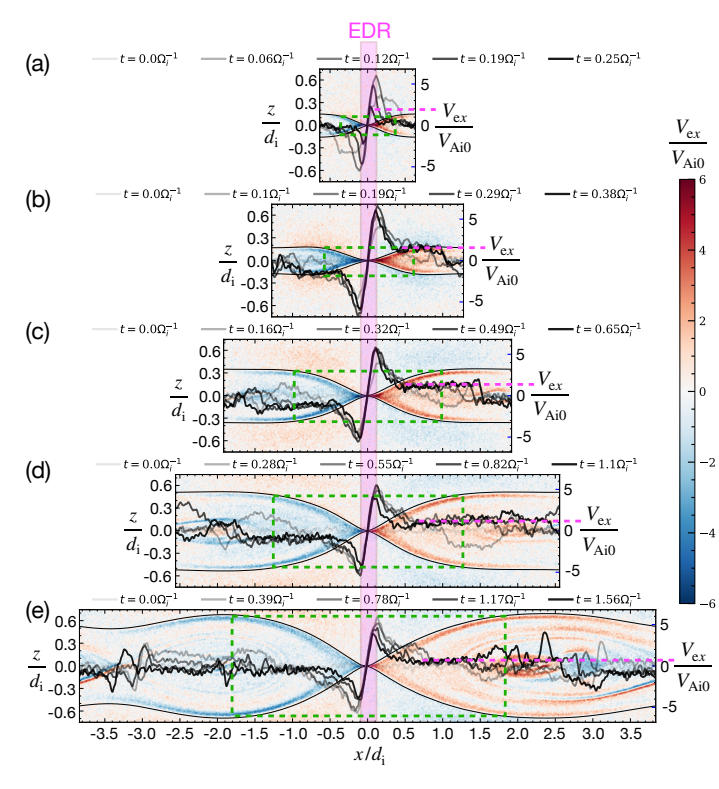


FIG. 2. Limiting speed of the flux transport. The time evolution of  $V_{ex}$  cuts at  $z{=}0$  overlaid on top of  $V_{ex}$  contour in simulations of box sizes (a)  $L_x = 1.28d_i$  (b)  $L_x = 2.56d_i$  (c)  $L_x = 3.84d_i$  (d)  $L_x = 5.12d_i$  (e)  $L_x = 7.68d_i$ . The value of these  $V_{ex}$  curves can be read by the axis at the right boundary of each panel and the magenta dashed horizontal line shows the representative plateau speed. The time of these  $V_{ex}$  cuts are shown on top of each panel while the time of the  $V_{ex}$  contour is marked by the corresponding transparent color circle in Fig. 1(e). The separatrices are marked in solid black. The red shaded band marks the electron diffusion region (EDR). The corners of the green boxes denote the locations downstream of which the exhaust opening angle quickly decreases to 0.

other four simulations of different system sizes, as shown in rest panels of Figure 2. Note that the plateau in the smallest system ( $L_x=1.28d_{\rm i}$ ) in Fig. 2(a) is less clear due to the back-pressure that will be discussed later. Overall, it is expected that a lower flux transport speed leads to a reconnection rate lower than the estimation in Eq. (1). We will denote this limiting speed as  $V_{\rm out,e}|_{L_0}$ , which is, the electron outflow speed at a distance  $L_0$  downstream of the X-line. Farther downstream of this location, the exhaust opening angle quickly decreases to 0, as marked in Fig. 1(b).

## B. The limiting speed of the flux transport

139

The first goal is to derive this limiting speed  $V_{\rm out,e}|_{L_0}$ .

We start from the electron momentum equation in the

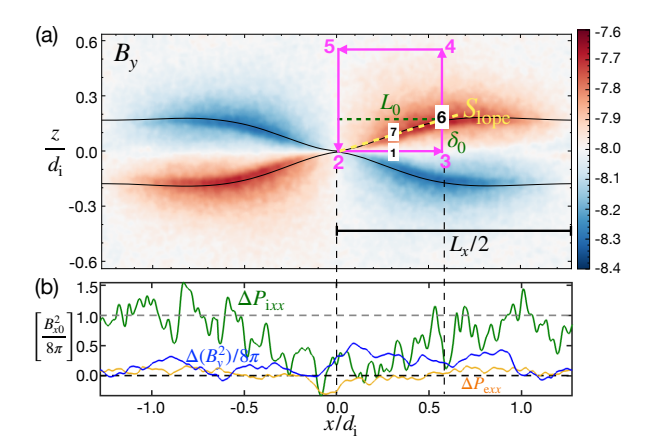


FIG. 3. Quantities critical to the estimation of the inplane electric field. (a) The out-of-plane magnetic field  $B_y$  (i.e., showing the Hall quadrupole signature) and the integral path of Eq. (4) in magenta. The black solid curves trace the magnetic separatrices. Critical points and the separatrix slope  $(S_{\text{lope}} = \delta_0/L_0)$  used in the analysis are annotated. (b) The difference of pressures from their upstream asymptotic values for components  $\Delta P_{ixx}$  (in green),  $\Delta P_{exx}$  (in yellow) and  $\Delta (B_y^2)/8\pi$  (in blue) along the z=0 line. For reference,  $B_{x0}^2/8\pi$  is plotted as the gray dashed horizontal line. While the oscillation in the  $\Delta P_{ixx}$  curve is unavoidable because of the noise in hot ions, the pressure depletion at the X-line is discernible.

142 steady state

$$nm_{\rm e}\mathbf{V}_{\rm e}\cdot\nabla\mathbf{V}_{\rm e} = \frac{\mathbf{B}\cdot\nabla\mathbf{B}}{4\pi} - \frac{\nabla B^2}{8\pi} - \mathrm{e}n\mathbf{E} - \nabla\cdot\mathbb{P}_{\rm e}.$$
 (2)

143 The term on the left-hand side (LHS) is the electron flow 144 inertia. The terms on the right-hand side (RHS) are the 145 magnetic tension force, magnetic pressure gradient force, 146 electric force, and the divergence of the electron pressure, 147 respectively. Note that the ion flow velocity  $|\mathbf{V}_{\rm i}| \ll {\rm elec}$ tron velocity  $|\mathbf{V}_{\rm e}|$  condition (i.e., ions do not carry the 149 electric current **J**) and Ampère's law were used to turn 150 the Lorentz force  $-e\mathbf{V}_{\mathrm{e}} \times \mathbf{B}/c \simeq \mathbf{J} \times \mathbf{B}/(nc)$  into the two magnetic forces in Eq. (2). Balancing the electron flow inertia with the magnetic tension  $\mathbf{B} \cdot \nabla \mathbf{B}/4\pi$  will lead to 153 an electron jet moving at the electron Alfvén speed. How-154 ever, the jet can be slowed down by other terms on the 155 RHS, especially the in-plane electric field E. One impor-156 tant source is the Hall electric field  $\mathbf{E}_{\mathrm{Hall}} = \mathbf{J} \times \mathbf{B}/enc$ 157 that arises from the separation of the lighter electron flows from the much heavier ion flows.  $\mathbf{E}_{\mathrm{Hall}}$  acts to slow down electrons and speed up ions to self-regulate itself [35]; thus, we expect  $E_x$  pointing in the same direction 161 as the outflows that slow down the electron jet [36, 37]. To quantify this phenomenon, we take the "finite-163 difference approximation" of Eq. (2) at point "1" in <sup>164</sup> Fig. 3(a). In the x-direction, the momentum equation 165 reads

$$\frac{nm_{\rm e}V_{\rm ex3}^2}{2L_0} \simeq \frac{B_{z1}}{4\pi\delta_0} 2B_{x7} - \frac{B_{z3}^2}{8\pi L_0} - enE_{x1},\tag{3}$$

where the targeted quantity  $V_{ex3}$  is  $V_{ex}$  at point "3", 167 etc. Being similar to the analysis from fig. 1(c) of Liu et 168 al. (2017) [38], this equation, moreover, includes the in-169 plane electric field critical to the acceleration of electron 170 outflows within the Hall region. This approach allows 171 one to derive the algebraic relation between key quanti-172 ties while considering the magnetic geometry of the sys-173 tem [35, 38–40]. Here we ignored the electron pressure gradient and the  $B_y^2$  gradient along path 2-3. These are justified since  $\Delta P_{\mathrm{ex}x}$  and  $\Delta (B_y^2)/8\pi$  are relatively small [37, 41] compared to  $B_{x0}^2/8\pi$  ( $\propto$  tension) in Fig. 3(b).

To estimate  $E_{x1}$ , we analyze the steady-state Faraday's law  $\oint \mathbf{E} \cdot d\vec{\ell} = 0$  and the original momentum equation along the closed loop (2-3-4-5-2) in Fig. 3(a). Unlike path <sup>180</sup> 2-3, the flow inertia  $|nm_{\rm e}\mathbf{V}_{\rm e}\cdot\nabla\mathbf{V}_{\rm e}|$  along the integral path 181 3-4-5-2 is negligible compared to  $|\mathbf{B}\cdot\nabla\mathbf{B}/4\pi-\nabla B^2/8\pi|=$  $_{182} |\mathbf{J} \times \mathbf{B}/c| \simeq |\mathrm{e}n\mathbf{V}_{\mathrm{e}} \times \mathbf{B}/c|,$  so we can write

$$c\int_{2}^{3} E_{x} dx = -c\int_{3452} \mathbf{E} \cdot d\vec{\ell} \simeq \int_{3}^{4} (V_{ex} B_{y} - \underbrace{V_{ey} B_{x}}) dz$$

$$+ \int_{4}^{5} (\underbrace{V_{ey} B_{z}} - V_{ez} B_{y}) dx + \int_{5}^{2} (\underbrace{V_{ex} B_{y}} - \underbrace{V_{ey} B_{x}}) dz. \tag{4}$$

vanishes because  $V_{\rm ex}=0$  along the inflow symmetry  $_{216}$  en $E_{x1}\simeq (P_{\rm i3}-P_{\rm i2})/L_0$  can be easily of the order of 185 line. Terms (a) and (d) roughly cancel each other be-186 cause  $\int V_{ey} B_x dz \propto \int J_y B_x dz \propto \int (\partial_z B_x) B_x dz = \Delta(B_x^2)/2$ , which is  $B_{x0}^2/2$  for the 3-4 and  $-B_{x0}^2/2$  for the 5-2 in-188 tegral paths. This equation can then be approximated 189 as

$$c\frac{E_{x1}}{2}L_0 \simeq V_{ex3} \int_3^6 B_y dz - B_{y0} \int_4^5 V_{ez} dx.$$
 (5)

190 The LHS used the fact that  $E_x$  increases monotonically 191 from 0 at the X-line to point "3". The first integral on 192 the RHS holds because the outflow  $V_{\rm ex}$  is narrowly con-193 fined within the separatrices. In the next step, we further approximate  $\int_3^6 B_y dz \simeq [(B_{y6} + B_{y3})/2] \delta_0$ . And, the 195 last integral  $\int_4^5 V_{\rm ez} dx \simeq \int_3^4 V_{\rm ex} dz \simeq V_{\rm ex3} \delta_0$ , since the par-196 ticle fluxes going through sides 2-3 and 2-5 are negligi-197 ble due to the symmetry shown in Fig. 3(a) and incom-198 pressibility is used. With the upstream  $B_{y0} \simeq B_{y3}$  as in 199 Fig. 3(a), we can then combine the two terms on the RHS 200 to derive

$$E_{x1} \simeq \frac{V_{ex3}}{c} (B_{y6} - B_{y3}) \frac{\delta_0}{L_0} \simeq \frac{4\pi ne}{c^2} \frac{\delta_0^2}{L_0} V_{ex3}^2.$$
 (6)

201 Here the last equality used Ampère's law  $(B_{y6}$  –  $_{202}$   $B_{y3})/\delta_0 \simeq (4\pi/c) neV_{ex3}$ . We note that the electric field  $_{203}$   $E_{x1}$  is basically determined by the convection of the Hall magnetic quadrupole field (i.e.,  $B_{y6}-B_{y3}$ ) and  $\int_{23452} \mathbf{E} \cdot \frac{1}{238} \frac{1}{B_{z3}} = \frac{1}{2} \frac{1}{B_{x7}} = \frac{1}{B_{x6}} \frac{1}{2}$ , and  $B_{x6} = B_{x0}$  from the mag $d\vec{\ell} = 0$ , as illustrated in Fig. 4(a).

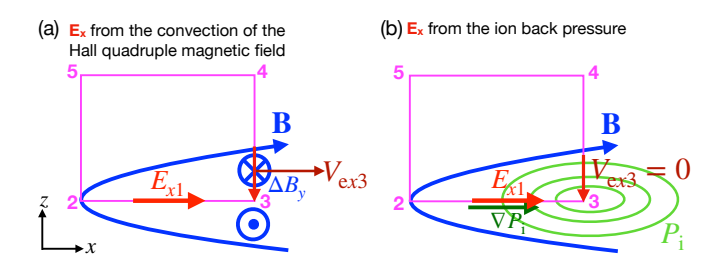


FIG. 4. Sources of the in-plane electric field  $E_{x1}$ . (a) The motional electric field  $-V_{\rm ex3}\Delta B_y/c$  arising from the convection of the Hall magnetic quadrupole field  $\Delta B_y \equiv B_y - B_g$ , combined with the steady-state Faraday's law  $\int_{23452} \mathbf{E} \cdot d\vec{\ell} = 0$ ; this corresponds to the  $f \to 0$  limit discussed in Eq. (7). (b) The ion back pressure accumulated within the plasmoid. Here the  $P_i$  contour is illustrated in green; this corresponds to the  $f \to 1$  limit discussed in in Eq. (7).

While this model mimics the characteristics of the electron current system of an idealized exhaust, it does not consider the effect of the closed boundary, which can be significant in a small system. In particular, the high ion pressure originating from the initial current sheet will 211 accumulate into the plasmoid at a fixed location. With 212 nearly immobile ions, where  $nm_{
m i}{f V}_{
m i}\cdot 
abla {f V}_{
m i}$  is negligible 213 compared to other forces in the ion momentum equa-214 tion, en**E**  $\simeq \nabla P_i$  [37, 41], as illustrated in Fig. 4(b). Term  $\bigcirc$  vanishes since  $V_{\rm ey}=0$  at the upstream; term  $_{215}$  In the small system size limit, one would expect that  $_{217}$   $B_{x0}^2/(8\pi L_0)$  due to the build-up of pressure within the  $_{218}$  plasmoid and the depletion of the pressure component 219 xx at the X-line [35], as shown by the central dip in the  $_{220} \Delta P_{ixx}$  (green) curve of Fig. 3(b).

> Hence, we will impose a reasonable condition where 222 the sum of the plasma and magnetic pressures completely 223 cancels the magnetic tension in the  $L_x \to 0$  limit. This 224 can be done by including this ion back pressure into the 225 full  $E_{x1}$  using a function  $f(L_x)$ ,

$$E_{x1} \simeq \frac{4\pi ne}{c^2} \frac{\delta_0^2}{L_0} V_{\text{ex3}}^2 + f \frac{B_{x0}^2 - B_{z3}^2}{8\pi L_0 ne}.$$
 (7)

<sup>226</sup> We choose  $f(L_x) = \operatorname{sech}(L_x/\Delta_f)$  so that, for  $L_x \gg \Delta_f$ 227 then  $f \to 0$ , corresponding to Fig. 4(a). For  $L_x \ll \Delta_f$ 228 then  $f \to 1$ , where the outflow is shut off and the ion 229 pressure gradient dominates, as in Fig. 4(b). The length 230 scale  $\Delta_f$  will later be determined to be  $\Delta_f = 1.28d_i$ , and the f-profile is shown in Fig. 5(b). The ion-electron inter-232 action is primarily mediated by the electric field within 233 the Hall region. Hence, it seems appropriate to heuris-234 tically include the effect of ion back pressure into the 235 electric field estimation.

Plugging Eq. (7) back to Eq. (3), and realizing <sup>237</sup>  $B_{z1} \simeq B_{z7} \simeq (\delta_0/L_0)B_{x7}$ , the separatrix slope  $S_{\text{lope}} \simeq \delta_0/L_0$ , 239 netic field line geometry (see the flux function contour

<sup>240</sup> in Fig. 1(a)), we obtain the limiting speed

$$V_{\text{out,e}}|_{L_0} = V_{\text{ex3}} \simeq \frac{d_{\text{i}}}{\delta_0} V_{\text{Ai0}} \sqrt{\frac{(1 - S_{\text{lope}}^2)(1 - f)}{2 + (d_{\text{e}}/\delta_0)^2}}.$$
 (8)

<sup>241</sup> A critical feature in Eq. (8) is  $V_{\text{out,e}}|_{L_0} \propto \delta_0^{-1}$ , which 242 provides a faster jet in a narrower exhaust. Without 243 the corrections gathered within the square root, if  $\delta_0 \rightarrow d_{\rm e}$ then  $V_{\rm out,e}|_{L_0}{
ightarrow}V_{\rm Ae0}$  (i.e., also true for  $\delta_0\ll d_{\rm e}$  when the electron inertial effect  $(d_e/\delta_0)^2$  within the square root is <sup>246</sup> retained). This is responsible for the faster flux transport <sup>247</sup> speed at sub-d<sub>i</sub>-scales, but it transitions to the ion Alfvén speed when  $\delta_0{ o}d_{
m i},$  because  $V_{{
m out,e}}|_{L_0}{ o}V_{{
m Ai0}},$  as in ioncoupled standard reconnection. In the limit  $\delta_0 \gg d_{\rm i}$ , one 250 needs to consider the full two-fluid equations [e.g., [42]], 251 coupling ions back to the scale larger than the typical ion diffusion region (IDR) size. The resulting  $V_{\text{out,e}}|_{L_0}$ remains ion Alfvénic [e.g.,[43]].

This scale-dependent velocity is the dispersive prop-255 erty discussed in the idea of Whistler/Kinetic Alfvén 256 wave (KAW)-mediated reconnection [28–30, 42, 44], but 257 here we also include the reduction by the back pressure 258 (parameterized by f) within a small system. The flow 259 is stopped when  $f \to 1$  in Eq. (8), corresponding to the <sub>260</sub> limit  $L_x \ll \Delta_f$  where the total pressure gradient com-<sub>261</sub> pletely cancels the tension force in Eq. (3). Finally, the 262 outflow speed is also reduced with a larger opening angle  $_{263}$  ( $S_{\text{lope}} \uparrow$ ).

### Geometry and reconnection rates

This limiting speed not only determines how fast mag-266 netic flux is convected into the outflow exhaust but also the upstream magnetic geometry and, thus, the strength of the reconnecting magnetic field immediately upstream of the EDR. All together, one can derive the electron-only

We closely follow the approach in Liu et al. (2022) [35] 272 to estimate the magnetic field strength  $B_{xe}$  immediately 314 curve. In a similar format, the limiting speed (Eq. (8)) is <sup>273</sup> upstream of the EDR of size  $2L_{\rm e} \times 2\delta_{\rm e}$ , as marked by the <sup>315</sup> shown in Fig. 5(c), while the more pronounced peak elec-274 red box in Fig. 1(b) and  $\delta_{\rm e} \sim d_{\rm e}$ . One can write

$$\frac{cE_{ye}}{B_{xe}V_{Ae}} = \frac{V_{\text{in,e}}}{V_{Ae}} \simeq \frac{\delta_{\text{e}}}{L_{\text{e}}} \sim \frac{\delta_{\text{0}}}{L_{0}} \simeq \frac{V_{\text{in,e}}|_{\delta_{0}}}{V_{\text{out,e}}|_{L_{0}}} = \frac{cE_{y}|_{\delta_{0}}}{B_{x0}V_{\text{out,e}}|_{L_{0}}}$$

where  $L_0$  and  $\delta_0$  are the exhaust length and half-width. 321 Overall, the green dashed curves already work reason-Other relevant quantities are annotated in Fig. 1(b). For 322 ably well for  $2.56d_i \le L_x \le 10d_i$  cases, but they over-277 instance,  $V_{\rm in,e}$  is the electron inflow speed at  $z=\delta_{\rm e}$  while 323 estimate quantities in the  $L_x=1.28d_{\rm i}$  case. For this  $V_{\rm in,e}|_{\delta_0}$  is the value at  $z=\delta_0$ . The first equality of Eq. (9) 324 reason, we set the length scale  $\Delta_f=1.28d_{\rm i}$  in  $f(L_x)$  to 279 used the frozen-in condition upstream of the EDR. The 325 parametrize the back pressure effect that suppresses the 280 second equality holds because of the incompressibility 326 outflow and rate. This corrects the predictions, and the  $_{281}$  and  $V_{ex,peak} \simeq V_{Ae}$ . The third equality approximates  $_{327}$  resulting black solid curves capture the scaling of these 282 the separatrix as a straight line to simplify the geometry. 328 key quantities in Fig. 5(a),(c),(d),(e); the quantitative 283 The fourth and fifth equalities used similar arguments to 329 agreements are within a factor of 2. Importantly, the the quantities at the edge of the larger  $L_0 \times \delta_0$  box. Fi- 330 rate (R) is now bounded by a value  $\simeq \mathcal{O}(1)$ , addressing

286 equality between the first and the last terms gives,

$$V_{\text{out,e}}|_{L_0} \simeq \frac{B_{xe}}{B_{x0}} V_{\text{Ae}} = \left(\frac{B_{xe}}{B_{x0}}\right)^2 \left(\frac{m_i}{m_e}\right)^{1/2} V_{\text{Ai0}}.$$
 (10)

<sup>287</sup> An important difference from Liu et al. (2022)[35] is that 288  $B_{xi}$  in their eq. (5) is now replaced by  $B_{x0}$ , since the 289 entire system is within the ion diffusion region (IDR).

Liu et al. (2022))[35] further estimated the depletion 291 of the pressure component along the inflow direction, 292 caused by the vanishing energy conversion  $\mathbf{J} \cdot \mathbf{E}_{\mathrm{Hall}} =$  $_{293}$  **J** · (**J** × **B**/nec) = 0; note that **E**<sub>Hall</sub> dominates within 294 the IDR and this pressure depletion provides the local-295 ization mechanism necessary for fast reconnection. One <sup>296</sup> can then use force balance along the inflow direction to <sup>297</sup> relate  $B_{xe}$  to the separatrix slope  $S_{lope}$  [35]. In the case  $_{298}$  where the guide field at the X-line does not change much 299 from its upstream value, like  $B_{u2}$  in Fig. 3, we get

$$\frac{B_{xe}}{B_{x0}} \simeq \frac{1 - 3S_{\text{lope}}^2}{1 + 3S_{\text{lope}}^2}.$$
(11)

300 The only difference is again that  $B_{xi}$  in eq. (9) of Liu et 301 al. (2022)[35] is now replaced by  $B_{x0}$ . In order to get the  $_{302}$  full solution from Eqs. (8),(10) and (11), one still needs 303 to relate  $\delta_0$  to  $S_{lope}$ . We approximate

$$\delta_0 = L_0 S_{\text{lope}} \sim 0.5 \left(\frac{L_x}{2}\right) S_{\text{lope}},$$
 (12)

 $_{304}$  as it is reasonable to expect  $2L_0$  to be on the order of the system size  $L_x$ , as in Fig. 1(b). We can then equate  $_{306}$  Eqs. (8) and (10) and solve for  $S_{\mathrm{lope}}$  numerically.

Once  $S_{\text{lope}}$  is determined, we can estimate the normal-

$$R \equiv \frac{cE_{\rm R}}{B_{x0}V_{\rm Ai0}} \simeq \frac{V_{\rm out,e}|_{L_0}B_{z3}}{B_{x0}V_{\rm Ai0}} \simeq \frac{V_{\rm out,e}|_{L_0}}{V_{\rm Ai0}}S_{\rm lope}.$$
 (13)

The last equality used  $B_{z3}/B_{x0} \simeq B_{z6}/B_{x6} \simeq S_{\text{lope}}$ . In 310 Fig. 5(a), the prediction of R as a function of  $L_x$  without 311 including the back pressure effect (i.e., f=0) is shown as 312 the green dashed curve, while the prediction with nonzero  $f(L_x)$  (given in Fig. 5(b)) is shown as the black solid 316 tron jet speed  $V_{\rm ex,peak} \simeq V_{\rm Ae} = (B_{xe}/B_{x0})(m_{\rm i}/m_{\rm e})^{1/2}V_{\rm Ai0}$ 317 is shown in Fig. 5(d). The estimated exhaust width  $\frac{cE_{y\mathrm{e}}}{B_{x\mathrm{e}}V_{\mathrm{Ae}}} = \frac{V_{\mathrm{in,e}}}{V_{\mathrm{Ae}}} \simeq \frac{\delta_{\mathrm{e}}}{L_{\mathrm{e}}} \sim \frac{\delta_{\mathrm{e}}}{L_{\mathrm{0}}} \sim \frac{V_{\mathrm{in,e}}|_{\delta_{\mathrm{0}}}}{V_{\mathrm{out,e}}|_{L_{\mathrm{0}}}} = \frac{cE_{y}|_{\delta_{\mathrm{0}}}}{B_{x\mathrm{0}}V_{\mathrm{out,e}}|_{L_{\mathrm{0}}}}, \\ \frac{cE_{y\mathrm{e}}}{B_{x\mathrm{0}}V_{\mathrm{out,e}}|_{L_{\mathrm{0}}}} \simeq \frac{V_{\mathrm{in,e}}|_{\delta_{\mathrm{0}}}}{V_{\mathrm{0}}} \simeq \frac{V_{\mathrm{in,e}}|_{\delta_{\mathrm{0}}}}{V_{\mathrm{0}}} = \frac{cE_{y}|_{\delta_{\mathrm{0}}}}{B_{x\mathrm{0}}V_{\mathrm{out,e}}|_{L_{\mathrm{0}}}}, \\ \frac{cE_{y\mathrm{e}}}{B_{x\mathrm{0}}V_{\mathrm{out,e}}|_{L_{\mathrm{0}}}} \simeq \frac{V_{\mathrm{in,e}}|_{\delta_{\mathrm{0}}}}{V_{\mathrm{0}}} \simeq \frac{V_{\mathrm{in,e}}|_{\delta_{\mathrm{0}}}}{V_{\mathrm{0}}} \simeq \frac{V_{\mathrm{in,e}}|_{\delta_{\mathrm{0}}}}{B_{x\mathrm{0}}V_{\mathrm{out,e}}|_{L_{\mathrm{0}}}}, \\ \frac{cE_{y\mathrm{e}}|_{\delta_{\mathrm{0}}}}{B_{x\mathrm{0}}V_{\mathrm{0}}} \simeq \frac{V_{\mathrm{in,e}}|_{\delta_{\mathrm{0}}}}{V_{\mathrm{0}}} \simeq \frac{V_{\mathrm{in,e}}|_{\delta_{\mathrm{0}}}}{V_{\mathrm{0}}} \simeq \frac{V_{\mathrm{in,e}}|_{\delta_{\mathrm{0}}}}{B_{x\mathrm{0}}V_{\mathrm{0}}}, \\ \frac{cE_{y\mathrm{e}}|_{\delta_{\mathrm{0}}}}{V_{\mathrm{0}}} \simeq \frac{V_{\mathrm{in,e}}|_{\delta_{\mathrm{0}}}}{V_{\mathrm{0}}} \simeq \frac{V_{\mathrm{in,e}}|_{\delta_{\mathrm{0}}}}{V_{\mathrm{0}}} \simeq \frac{V_{\mathrm{in,e}}|_{\delta_{\mathrm{0}}}}{V_{\mathrm{in,e}}} \simeq \frac{V_{in,e}|_{\delta_{\mathrm{0}}}}{V_{\mathrm{in,e}}} \simeq \frac{V_{\mathrm{in,e}}|_{\delta_{\mathrm{0}}}}{V_{i$ (9)  $_{320}$  from Figs. 1(e) and 2.

285 nally, in the 2D steady-state,  $E_y$  is uniform. Thus, the 331 the key question that motivates this work.

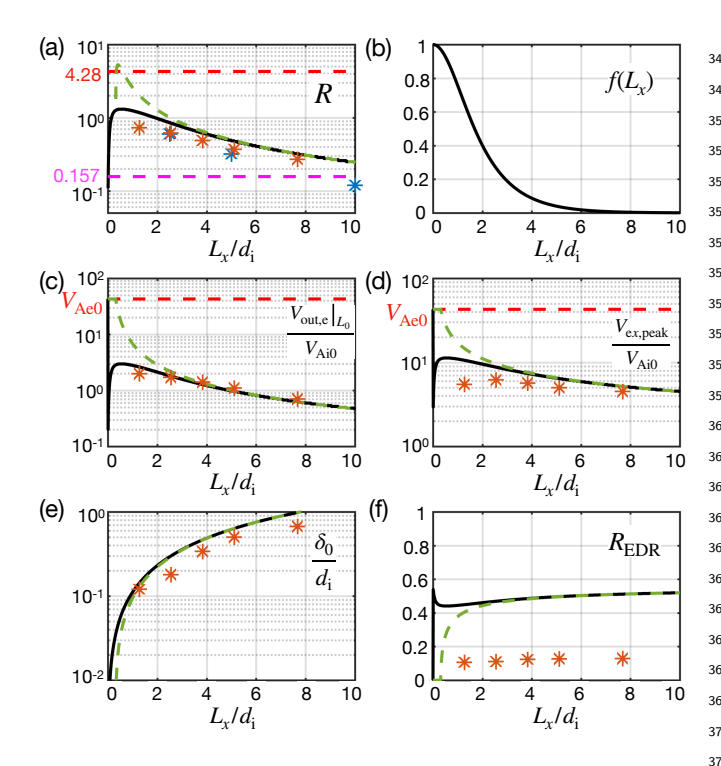


FIG. 5. Predictions as a function of the system size  $L_x$ . (a) The normalized reconnection rate. (b) The profile  $f(L_x) = \operatorname{sech}(L_x/1.28d_i)$  used for the black solid curves in other panels. (c) The limiting speed of flux transport. (d) The peak electron outflow speed. (e) The exhaust halfthickness. (f) The rate normalized to the electron diffusion region (EDR) quantities. The predictions with  $f(L_x)$  in (b) are shown as the black solid curves, while the green dashed curves have f = 0. Orange symbols are from the PIC simulations carried out in this paper. In panel (a), the blue symbols are from Pyakurel et al. [6]. For comparison, the rough prediction from Eq. (1) is marked by the red dashed horizontal line, and R = 0.157 predicted for ion-coupled standard reconnection [35] as the magenta dashed horizontal line. In panels (c) and (d), the maximum plausible electron outflow value,  $V_{\text{Ae0}}$ , is marked as red horizontal dashed lines.

#### **DISCUSSION** III.

332

A framework for predicting the electron-only reconnection rate (Eqs. (8),(10),(11),(12) and (13)) is developed after recognizing the difference in the EDR-scale and the asymptotic regions, considering both the inflow and outflow force-balances within the ion inertial scale. This simple model not only provides reasonable predictions for the simulated rates in kinetic plasmas but also captures the scaling of various key quantities in PIC simulations of different sizes (Fig. 5). We find that the in-plane electric field (Fig. 4) regulates the electron outflow speed and thus the reconnection rates. It is worth mentioning that this model has successfully integrated the idea of Whistler/KAW-mediated reconnection [28–30, 42, 44] into the reconnection rate model [35].

348 to determine the far upstream, asymptotic magnetic 349 field  $B_{x0}$  using the short-scaled tetrahedron formation. 350 Practically, it is more accessible to obtain the rate 351 normalized by the local quantities around the EDR,  $_{352}$   $R_{\rm EDR} \equiv cE_{\rm R}/(B_{xe}V_{\rm Ae}) \simeq (B_{xe}/B_{x0})^{-2} (m_{\rm i}/m_{\rm e})^{-1/2} R.$ Our theory in Fig. 5(f) predicts a nearly constant  $_{354}$   $R_{\rm EDR} \sim 0.4$ -0.5. In Fig. 1(d), one  $d_{\rm e}$  upstream of the 355 X-line is close to the location of the peak electron inflow 356 speed and features the upstream edge of the EDR that  $_{357}$  MMS can easily identify [34, 45, 46]. The resulting  $R_{\rm EDR}$ 358 (orange symbols in Fig. 5(f)) based on the measured <sub>359</sub>  $B_{xe}$  at  $z=1d_e$  are four times lower (i.e.,  $R_{\rm EDR}\simeq 0.1$ ) [47]. However, we also note that the  $B_x$  at the location where  $V_{\rm ex,peak} = V_{\rm Ae}$  holds accurately is roughly twice 362 smaller than  $B_{xe}$  because of the sharp  $B_x$  profile at  $_{363}$   $d_{\mathrm{e}}\text{-scales}$  (i.e., note that this profile is proportional to the  $B_x/\sqrt{4\pi n_{\rm e}m_{\rm e}}$  profile in Fig. 1(d) because of the 365 constancy of  $n_e$ ). If we take this  $B_x$  as  $B_{xe}$ , the factorof-two difference results in a four-times higher  $R_{\rm EDR}$ , 367 which may explain this discrepancy. Despite this extra 368 complexity, our simple theory captures the constancy of the simulated  $R_{\rm EDR}$ . Recent MMS observational reports 370 of electron-only reconnection indicate rates around 0.25 [45, 46]. Another event at the magnetopause suggests 372 an even higher reconnection rate, up to  $\sim 0.4$  during the onset phase [48].

Even with a strong guide field ( $|B_g|=8B_{x0}$ ) in our sim-<sub>375</sub> ulation, the ion gyro-radius  $\rho_i$ =1.23 $d_i$  due to the high ion 376 temperature  $(T_{i0} = 115.16m_iV_{Ai0}^2)$ . Guan et al. (2023) [24] studied cases of guide fields  $B_g=1B_{x0}$  and  $8B_{x0}$ , and they concluded that the  $|\mathbf{V}_{\mathrm{i}}| \ll |\mathbf{V}_{\mathrm{e}}|$  condition is met when the system size is smaller than the ion gyroradius  $(\rho_i)$ . Presumably, because with a high ion thermal speed  $_{381}$  (10.73 $V_{\rm Ai0}$  in our runs) and large gyro-radii, ions will be  $_{382}$  quickly gyrated out of the region of constant **E**, avoiding the formation of coherent ion flows through direct acceleration over a longer time span [49]. Our analytical the-385 ory is built on this  $|\mathbf{V}_{\mathrm{i}}| \ll |\mathbf{V}_{\mathrm{e}}|$  condition (i.e., ions do not 386 carry currents as in the EMHD limit [50-52])), and it ex-387 plains the transition to the standard reconnection rate at <sub>388</sub>  $L_x \gtrsim 10d_i$ , as shown by Pyakurel et al. (2019) [6]. Under 389 this same condition, the analytical approach (and thus 390 the predictions) derived here also works for anti-parallel 391 reconnection and is not limited to the strong guide field case.

Caveats should be kept in mind when applying these 394 predictions. Related to the above discussion, our the-395 ory does not model the lower rate reported with a small 396 ion gyro-radius  $\rho_{\rm i}$  ( $\ll L_x$ ) where ion currents emerge, 397 as reported in Guan et al. (2023) [24]. Bessho et al. 398 (2022) [12] found  $cE_{\mathrm{R}}/(B_{x0}V_{\mathrm{ex,peak}})$  ranging from 0.1 to 399 0.7 in the turbulent shock transition region, indicating 400 the possibility of a much higher rate, potentially due 401 to the driving of high-speed background flows. In addi-402 tion, with a non-periodic, open outflow system, such as 403 the merger between isolated small-scale magnetic islands, 404 electron-only reconnection therein may not saturate early For in-situ MMS observations, it might be challenging 405 due to the back pressure and may achieve a higher rate

 $_{406}$  ( $R \simeq 4.28$ ) as predicted by the green dashed curves in  $_{438}$  favorable to the occurrence of electron-only reconnection <sup>407</sup> Fig. 5(a). Finally, the thickness-dependent growth rate of <sup>439</sup> (see the "Discussion" section). The simulation sizes are the tearing instability in this regime may also contribute  $440~L_x \times L_z = 1.28d_i \times 2.56d_i, 2.56d_i \times 2.56d_i, 3.84d_i \times 3.84d_i,$ 409 to its onset and the early development of electron-only 441  $5.12d_i \times 5.12d_i$  and  $7.68d_i \times 7.68d_i$ , with cell size  $0.21d_e$ 410 reconnection [49, 53–56]. Together with the time depen-442 and time step  $2.5 \times 10^{-5} \Omega_{\rm ci}^{-1}$ . The particle number per 411 dence and the full 3D nature [57], future endeavors are 443 cell is 6000. Periodic boundaries are used. In our figures, 412 required to develop a more complete theory. Neverthe-414 we show the top current sheet with our coordinate origin 413 less, our simple model demonstrates a working frame- 445 re-centered at the X-line. 414 work addressing critical features that necessitate faster 415 electron-only reconnection rates.

#### METHODS IV.

416

462

463

464

465

466

467

468

469

470

471

472

473

474

475

476

481

482

We carry out 2D PIC simulations of magnetic re-418 connection in proton-electron plasmas with mass ratio  $m_{\rm i}/m_{\rm e} = 1836$  using the P3D code [58]. We em-420 ploy the setup of case A in Pyakurel et al., 2019 [6]. 421 which is designed based on parameters of the MMS 422 electron-only event [2], but with five different system 423 sizes. The double Harris sheet profile  $\mathbf{B} = B_{x0} [\tanh(z 424 \ 0.25L_z/w_0) - \tanh(z - 0.75L_z/w_0) - 1]\hat{x} + B_g\hat{y}$  is em-<sub>425</sub> ployed, with a uniform guide field  $B_{\rm g} = -8.0 B_{x0}$ . The 426 initial half thickness  $w_0 = 0.06d_{\rm i}$  where the ion inertial scale  $d_i \equiv (m_i c^2/4\pi n_0 e^2)^{1/2}$  is normalized to the 428 upstream density  $n_0$ . The in-plane ion Alfvén speed 429  $V_{\rm Ai0}=B_{x0}/(4\pi n_0 m_{\rm i})^{1/2}$  and cyclotron frequency  $\Omega_{\rm ci}\equiv$  $_{430}$  e $B_{x0}/m_{\rm i}c$  are normalized to the reconnecting component  $^{431}$   $B_{x0}$ . The speed of light  $c=300V_{\rm Ai0}$ . The high temper- $^{432}$  ature  $T_{\rm i0}=115.16m_{\rm i}V_{\rm Ai0}^2$  and  $T_{\rm e0}=11.51m_{\rm i}V_{\rm Ai0}^2$  result  $^{433}$  in  $\beta_{\rm i}=8\pi n_0T_{\rm i0}/(B_{x0}^2+B_{\rm g}^2)=3.54$  and  $\beta_{\rm e}=0.35$ , and  $^{434}$  a nearly uniform density from pressure balance condi-435 tion. The ratio of gyro-radius (based on the full field 436 strength) and inertial length are  $ho_{\rm i}/d_{\rm i} \simeq 1.33$  for ions <sub>437</sub> and  $\rho_{\rm e}/d_{\rm e} \simeq 0.42$  for electrons. This  $T_{\rm i} \gg T_{\rm e}$  limit is

## DATA AVAILABILITY

Access  $_{
m to}$ the simulation  $_{
m data}$ scripts 448 used to plot the figures are available at Zenodo (https://doi.org/10.5281/zenodo.14919784). data are available from the corresponding author upon 451 reasonable request.

### CODE AVAILABILITY

The P3D code is available through collaboration with 454 the second author, P. S. Pyakurel. Upon request, the 455 code's developer grants access to and helps run the 456 simulations and handle the output data. The simulation 457 data are analyzed using IDL and Python. The scripts to 458 read the output data are available at the data storage 459 site Zenodo.org.

### REFERENCES

- [1] J. L. Burch, T. E. Moore, R. B. Torbert, and B. L. Giles. Magnetospheric Multiscale Overview and Science Objectives. Space Sci. Rev., 199(1-4):5-21, March 2016.
- T. D. Phan, J. P. Eastwood, M. A. Shay, J. Drake, B. U. Ö. Sonnerup, M. Fujimoto, P. A. Cassak, M. Øieroset, J. L. Burch, R. B. Torbert, A. C. Rager, J. C. Dorelli, D. J. Gershman, C. Pollock, P. S. 489 Pyakurel, C. C. Haggerty, Y. Khotyaintsev, B. Lavraud, 490 Y. Saito, M. Oka, R. E. Ergun, A. Retino, O. Le Contel, 491 M. R. Argall, B. L. Giles, T. E. Moore, F. D. Wilder, R. J. Strangeway, C. T. Russell, P. A. Lindqvist, and 493 W. Magnes. Electron magnetic reconnection without ion 494 coupling in Earth's turbulent magnetosheath. *Nature*, 495 557(7704):202-206, May 2018.
- J. E. Stawarz, J. P. Eastwood, T. D. Phan, I. L. Gin-497 gell, M. A. Shay, J. L. Burch, R. E. Ergun, B. L. Giles, 498 D. J. Gershman, O. Le Contel, P. A. Lindqvist, C. T. 499 Russell, R. J. Strangeway, R. B. Torbert, M. R. Argall, 500 D. Fischer, W. Magnes, and L. Franci. Properties of the 501 Turbulence Associated with Electron-only Magnetic Re- 502 connection in Earth's Magnetosheath. ApJL, 877(2):L37, 503

June 2019.

- J. E. Stawarz, J. P. Eastwood, T. D. Phan, I. L. Gingell, P. S. Pyakurel, M. A. Shay, S. L. Robertson, C. T. Russell, and O. Le Contel. Turbulence-driven magnetic reconnection and the magnetic correlation length: Observations from Magnetospheric Multiscale in Earth's magnetosheath. Physics of Plasmas, 29(1):012302, January
- [5] D. S. Payne, M. Swisdak, J. P. Eastwood, J. F. Drake, P. S. Pyakurel, and J. R. Shuster. In-situ observations of the magnetothermodynamic evolution of electron-only reconnection. Communications Phys., 8:36, 2025.
- [6] P. S. Pyakurel, M. A. Shay, T. D. Phan, W. H. Matthaeus, J. F. Drake, J. M. TenBarge, C. C. Haggerty, K. C. Klein, P. A. Cassak, T. N. Parashar, M. Swisdak, and A. Chasapis. Transition from ion-coupled to electron-only reconnection: Basic physics and implications for plasma turbulence. Phys. Plasmas, 26:082307,
- Francesco Califano, Silvio Sergio Cerri, Matteo Faganello, Dimitri Laveder, Manuela Sisti, and Matthew W.

Kunz. Electron-only reconnection in plasma turbulence. 568 Frontiers in Physics, 8:317, September 2020.

569

582

588

602

603

604

609

504 505

506

507

508

509

510

511

512

513

514

515

- Luca Franci, Emanuele Papini, Alfredo Micera, Giovanni Lapenta, Petr Hellinger, Daniele Del Sarto, David 571 Burgess, and Simone Landi. Anisotropic Electron Heating in Turbulence-driven Magnetic Reconnection in the 573 Near-Sun Solar Wind. Astrophys. J., 936(1):27, September 2022.
- Zhuo Liu, Calo Silva, Lucio M. Milanese, Muni Zhou, 576 Noah R. Mandell, and Nuno F. Loureiro. Electrononly reconnection and inverse magnetic-energy transfer at sub-ion Scales. submitted. arXiv:2407.06020, 2024.
- I. Gingell, S. J. Schwartz, J. P. Eastwood, J. L. Burch, 516 R. E. Ergun, S. Fuselier, D. J. Gershman, B. L. Giles, 517 Y. V. Khotyaintsev, B. Lavraud, P. A. Lindqvist, W. R. 518 Paterson, T. D. Phan, C. T. Russell, J. E. Stawarz, R. J. 519 Strangeway, R. B. Torbert, and F. Wilder. Observations 520 of Magnetic Reconnection in the Transition Region of 521 Quasi-Parallel Shocks. Geophys. Res. Lett., 46(3):1177-522 1184, February 2019. 523
- Shan Wang, Li-Jen Chen, Naoki Bessho, Michael Hesse, 524 Lynn B. Wilson, Barbara Giles, Thomas E. Moore, 525 Christopher T. Russell, Roy B. Torbert, and James L. 526 Burch. Observational Evidence of Magnetic Reconnec-527 tion in the Terrestrial Bow Shock Transition Region. Geophys. Res. Lett., 46(2):562-570, January 2019. 529
- N. Bessho, L. J. Chen, J. E. Stawarz, S. Wang, M. Hesse, 530 L. B. Wilson, and J. Ng. Strong reconnection electric 531 fields in shock-driven turbulence. Physics of Plasmas, 532 29(4):042304, April 2022. 533
- Terry Z. Liu, San Lu, Drew L. Turner, Imogen Gingell, [13] 534 Vassilis Angelopoulos, Hui Zhang, Anton Artemyev, and 599 535 James L. Burch. Magnetospheric Multiscale (MMS) Ob- 600 536 servations of Magnetic Reconnection in Foreshock Tran- 601 537 sients. Journal of Geophysical Research (Space Physics). 538 125(4):e27822, April 2020. 539
- Rongsheng Wang, Quanming Lu, Rumi Nakamura, Wolf-540 gang Baumjohann, Can Huang, Christopher T. Russell, 605 541 J. L. Burch, Craig J. Pollock, Dan Gershman, R. E. Er- 606 542 gun, Shui Wang, P. A. Lindqvist, and Barbara Giles. An 607 543 Electron-Scale Current Sheet Without Bursty Reconnec- 608 544 tion Signatures Observed in the Near-Earth Tail. Geo-545 phys. Res. Lett., 45(10):4542-4549, May 2018. 546
- S. Lu, R. Wang, Q. Lu, V. Angelopoulos, R. Nakamura, 611 547 548 A. V. Artemyev, P. L. Pritchett, and T. Z. Liu et al. Magnetotail reconnection onset caused by electron kinetics 613 549 with a strong external driver. Nat. Commun., 11:5049, 614 550 2020.551
- M. Hubbert, C. T. Russell, Yi Qi, S. Lu, J. L. Burch, 616 [16] 552 B. L. Giles, and T. E. Moore. Electron-Only Recon- 617 553 nection as a Transition Phase From Quiet Magnetotail 618 554 Current Sheets to Traditional Magnetotail Reconnec- 619 555 tion. Journal of Geophysical Research (Space Physics), 620 556 127(3):e29584, March 2022. 557
- H. Y. Man, M. Zhou, Y. Y. Yi, Z. H. Zhong, A. M. 622 558 Tian, X. H. Deng, Y. Khotyaintsev, C. T. Russell, and 623 559 B. L. Giles. Observations of Electron-Only Magnetic Re- 624 560 connection Associated With Macroscopic Magnetic Flux 625 561 Ropes. Geophys. Res. Lett., 47(19):e89659, October 2020. 626 562
- C. Norgren, D. B. Graham, Yu. V. Khotyaintsev, 627 563 M. André, A. Vaivads, M. Hesse, E. Eriksson, P. A. 628 564 Lindqvist, B. Lavraud, J. Burch, S. Fuselier, W. Magnes, 629 565 D. J. Gershman, and C. T. Russell. Electron Recon-566 nection in the Magnetopause Current Layer. Journal 567

- of Geophysical Research (Space Physics), 123(11):9222-9238, November 2018.
- A. T. Marshall, J. L. Burch, P. H. Reiff, J. M. Webster, 570 [19] R. B. Torbert, R. E. Ergun, C. T. Russell, R. J. Strangeway, B. L. Giles, R. Nakamura, K. J. Hwang, and K. J. Genestreti. Asymmetric Reconnection Within a Flux Rope-Type Dipolarization Front. Journal of Geophysical Research (Space Physics), 125(1):e27296, January 2020.
  - Peivun Shi, Prabhakar Srivastav, M. Hasan Barbhuiya, Paul A. Cassak, Earl E. Scime, and M. Swisdak. Laboratory Observations of Electron Heating and Non-Maxwellian Distributions at the Kinetic Scale during Electron-Only Magnetic Reconnection. Phys. Rev. Lett., 128(2):025002, January 2022.
  - S. Greess, J. Egedal, A. Stanier, J. Olson, W. Daughton, A. Lê, A. Millet-Ayala, C. Kuchta, and C. B. For-Kinetic simulations verifying reconnection rates measured in the laboratory, spanning the ion-coupled to near electron-only regimes. Physics of Plasmas, 29(10):102103, October 2022.
  - [22] Abraham Chien, Lan Gao, Shu Zhang, Hantao Ji, Eric G. Blackman, William Daughton, Adam Stanier, Ari Le, Fan Guo, Russ Follett, Hui Chen, Gennady Fiksel, Gabriel Bleotu, Robert C. Cauble, Sophia N. Chen, Alice Fazzini, Kirk Flippo, Omar French, Dustin H. Froula, Julien Fuchs, Shinsuke Fujioka, Kenneth Hill, Sallee Klein, Carolyn Kuranz, Philip Nilson, Alexander Rasmus, and Ryunosuke Takizawa. Non-thermal electron acceleration from magnetically driven reconnection in a laboratory plasma. Nature Physics, 19(2):254-262, February
  - [23] Peivun Shi, Earl E. Scime, M. Hasan Barbhuiya, Paul A. Cassak, Subash Adhikari, M. Swisdak, and Julia E. Stawarz. Using direct laboratory measurements of electron temperature anisotropy to identify the heating mechanism in electron-only guide field magnetic reconnection. Phys. Rev. Lett., 131:155101, Oct 2023.
  - Yundan Guan, Quanming Lu, San Lu, Kai Huang, and Rongsheng Wang. Reconnection Rate and Transition from Ion-coupled to Electron-only Reconnection. Astrophys. J., 958(2):172, December 2023.
  - [25] M. Hesse, T. Neukirch, K. Schindler, M. Kuznetsova, and S. Zenitani. The diffusion region in collisionless magnetic reconnection. Space Sci. Rev., 160:3–23, 2011.
  - H. J. Cai and L. C. Lee. The generalized Ohm's law in collisionless magnetic reconnection. Phys. Plasmas, 4(3):509-520, 1997.
  - V. M. Vasyliunas. Theoretical models of magnetic field line merging, 1. Rev. Geophys. Space Phys., 13(1):303, 1975.
  - M. E. Mandt, R. E. Denton, and J. F. Drake. Transition to whistler mediated reconnection. Geophys. Res. Lett., 21(1):73-76, 1994.
- 621 [29] M. A. Shay, J. F. Drake, B. N. Rogers, and R. E. Denton. The scaling of collisionless, magnetic reconnection for large systems. *Geophys. Res. Lett.*, 26(14):2163–2166,
  - B. N. Rogers, R. E. Denton, J. F. Drake, and M. A. Shay. Role of dispersive waves in collisionless magnetic reconnection. Phys. Rev. Lett., 87(19):195004, 2001.
  - P. A. Cassak, Yi-Hsin Liu, and M. A. Shay. A review of the 0.1 reconnection rate problem. J. Plasma Phys., 83:715830501, 2017.

- [32] T. K. M. Nakamura, K. J. Genestreti, Y. H. Liu, R. Naka-631 mura, W. L. Teh, H. Hasegawa, W. Daughton, M. Hesse, 632 R. B. Torbert, J. L. Burch, and B. L. Giles. Measurement 633 of the Magnetic Reconnection Rate in the Earth's Magne-634 totail. Journal of Geophysical Research (Space Physics), 635 123(11):9150-9168, November 2018. 636
- K. J. Genestreti, T. K. M. Nakamura, R. Nakamura, 637 R. E. Denton, R. B. Torbert, J. L. Burch, F. Plaschke, 638 S. A. Fuselier, R. E. Ergun, B. L. Giles, and C. T. Rus-639 sell. How Accurately Can We Measure the Reconnection 640 Rate  $E_M$  for the MMS Diffusion Region Event of 11 July 641 2017? Journal of Geophysical Research (Space Physics), 642 123(11):9130-9149, November 2018. 643
- K. R. Pritchard, J. L. Burch, S. A. Fuselier, K. J. Gen-644 estreti, R. E. Denton, J. M. Webster, and J. M. Broll. Re-645 connection Rates at the Earth's Magnetopause and in the 646 Magnetosheath. Journal of Geophysical Research (Space 647 Physics), 128(9):e2023JA031475, September 2023. 648
- Yi-Hsin Liu, P. Cassak, X. Li, M. Hesse, S-C Lin, and 649 K. Genestreti. First-principle theory of the rate of mag- 714 650 651 netic reconnection in magnetospheric and solar plasmas. Communications Phys., 5:97, 2022. 652
- [36] Yi-Hsin Liu, M. Hesse, R. Genestreti, and J. Burch et al. 717 653 Ohm's Law, the Reconnection Rate, and Energy Conver-718 654 sion in Collisionless Magnetic Reconnection. Space Sci. 719 Rev., 221(43):16, 2025. 656
- Y. Guan, Q. Lu, S. Lu, Y. Shu, and R. Wang. Role of 721 657 Ion Dynamics in Electron-Only Magnetic Reconnection. 722 658 Geophys. Res. Lett., 51:e2024GL110787, 2024.
- Yi-Hsin Liu, M. Hesse, F. Guo, W. Daughton, H. Li, P. A. 724 [38] 660 Cassak, and M. A. Shay. Why does steady-state magnetic 725 [52] 661 reconnection have a maximum local rate of order 0.1? 726 662 Phys. Rev. Lett., 118:085101, 2017. 663
- [39] 664 S. Wang, and L.-J. Chen. On the collisionless asym- 729 665 metric magnetic reconnection rate. Geophys. Res. Lett., 730 666 45:3311, 2018. 667
- Xiaocan Li and Yi-Hsin Liu. The effect of thermal pres- 732 [54] 668 sure on collisionless magnetic reconnection rate. Astro-733 669 phys. J., 912:152, 2021. 670
- J. R. Wygant, C. A. Cattell, R. Lysak, Y. Song, 735 671 J. Dombeck, J. McFadden, F. S. Mozer, C. W. Carlson, 736 672 G. Parks, E. A. Lucek, A. Balogh, M. Andre, H. Reme, 737 673 M. Hesse, and C. Mouikis. Cluster observations of an in- 738 674 675 tense normal component of the electric field at a thin re- 739 connecting current sheet in the tail and its role in shock- 740 676 like acceleration of the ion fluid into the separatrix region. 741 677 J. Geophys. Res., 110:A09206, 2005. 678
- [42] P. A. Cassak. Catastrophe model for the onset of fast 743 [57] 679 magnetic reconnection. PhD thesis, University of Mary-744 680 681
- Yi-Hsin Liu, J. F. Drake, and M. Swisdak. The struc- 746 682 ture of magnetic reconnection exhaust boundary. Phys. 747 [58] 683 Plasmas, 19, 2012. 684
- J. F. Drake, M. A. Shay, and M. Swisdak. The Hall 749 685 fields and fast magnetic reconnection. Phys. Plasmas, 750 686 15(4), 2008. 687
- J. L. Burch, J. M. Webster, M. Hesse, K. J. Genestreti, 688 and R. E. Denton et al.,. Electron inflow velocities and 689 reconnection rates at earth's magnetopause and magne-690 tosheath. Geophy. Res. Lett., 47:e2020GL089082, 2020. 691
- [46] P. S. Pyakurel, T. D. Phan, J. F. Drake, M. A. Shay, 752 692 693 694

- R. J. Strangeway, and C. T. Russell. On the Short-scale Spatial Variability of Electron Inflows in Electron-only Magnetic Reconnection in the Turbulent Magnetosheath Observed by MMS. Astrophys. J., 948(1):20, May 2023.
- A. M. Dimits, G. Bateman, M. A. Beer, B. I. Cohen, W. Dorland, G. W. Hammett, C. Kim, J. E. Kinsey, M. Kotschenreuther, A. H. Kritz, L. L. Lao, J. Mandrekasand W. M. Nevins, S. E. Parker, A. J. Redd, D. E. Shumaker, R. Sydora, and J. Weiland. Comparisons and physics basis of tokamak transport models and turbulence simulations. Phys. Plasmas, 7:969, 2000.

699

705

706

708

748

- P. S. Pyakurel, T. D. Phan, M. Øieroset, J. F. Drake, M. A. Shay, A. Mallet, J. Stawarz, S. Wang, K. Oka, K. J. Genestreti, N. Ahmadi, J. L. Burch, R. B. Tobert, R. E. Ergun, D. J Gershman, B. L. Giles, and R. J. Strangeway. Detection of large guide field electron-only reconnection in a filamentary current sheet immersed in a large-scale magnetopause reconnection exhaust. Phys. Rev. Lett., 2025.
- Cheng-Yu Fan, Shan Wang, Xu-Zhi Zhou, San Lu, Lu Quanming, Prayash Pyakurel, Qiugang Zong, and Zhi-Yang Liu. New Insights on the High Reconnection Rate and the Diminishment of Ion Outflow. submitted. arXiv:2411.13352, 2024.
- S. V. Bulanov, F. Pegoraro, and A. S. Sakharov. Magnetic reconnection in electron magnetohydrodynamics. Physics of Fluids B, 4(8):2499–2508, August 1992.
- Neeraj Jain and A. Surjalal Sharma. Electron scale structures in collisionless magnetic reconnection. Physics of Plasmas, 16(5):050704, May 2009.
- Neeraj Jain and A. Surjalal Sharma. Evolution of electron current sheets in collisionless magnetic reconnection. Physics of Plasmas, 22(10):102110, October 2015.
- Yi-Hsin Liu, M. Hesse, P. A. Cassak, M. A. Shay, 728 [53] H. Betar, D. Del Sarto, M. Ottaviani, and A. Ghizzo. Microscopic scales of linear tearing modes: a tutorial on boundary layer theory for magnetic reconnection. Journal of Plasma Physics, 88(6):925880601, December 2022.
  - H. Betar and D. Del Sarto. Asymptotic scalings of fluid, incompressible "electron-only" reconnection instabilities: Electron-magnetohydrodynamics tearing modes. Physics of Plasmas, 30(7):072111, July 2023.
  - Alfred Mallet. The onset of electron-only reconnection. Journal of Plasma Physics, 86(3):905860301, June 2020.
  - Olga O. Tsareva, Makar V. Leonenko, Elena E. Grigorenko, Helmi V. Malova, Victor Yu. Popov, and Lev M. Zelenyi. Fast Tearing Mode Driven by Demagnetized Electrons. Geophys. Res. Lett., 51(8):e2023GL106867, April 2024.
  - P. S. Pyakurel, M. A. Shay, J. F. Drake, T. D. Phan, P. A. Cassak, and J. L. Verniero. Faster Form of Electron Magnetic Reconnection with a Finite Length X-Line. Phys. Rev. Lett., 127(15):155101, October 2021.
  - A. Zeiler, D. Biskamp, J. F. Drake, B. N. Rogers, M. A. Shay, and M. Scholer. Three-dimensional particle simulations of collisionless magnetic reconnection. J. Geophys. Res., 107(A9):1230, 2002.

# ACKNOWLEDGMENTS

Y.L. is grateful for support from NASA's MMS mis-M. Øieroset, C. C. Haggerty, J. Stawarz, J. L. Burch, 753 sion 80NSSC21K2048 and NSF Career Award 2142430. R. E. Ergun, D. J. Gershman, B. L. Giles, R. B. Torbert, 754 P.P. is supported by NASA MMS early career grant 755 80NSSC21K1481 and NASA grant 80NSSC24K0559. We 765 X.L. and S.T. carried out additional simulations confirm-758 NCAR's Computational and Information Systems Lab- 768 authors discussed and commented on the paper. 759 oratory, sponsored by the National Science Foundation 760 (NSF), and NERSC Advanced Supercomputing, spon-761 sored by the Department of Energy (DOE).

would like to acknowledge the high-performance com- 766 ing the general conclusion. M.H. and N.B. provided theputing support from Derecho, which is provided by 767 oretical inputs. K. G. provides observational inputs. All

#### COMPETING INTERESTS X.

The authors declare no competing interests.

771

## **AUTHOR CONTRIBUTIONS**

762

Y.L. derived the theory and wrote the paper. P.P. car-764 ried out the simulation and analysis shown in this paper.